RESEARCH ARTICLE

ADVANCED
PHOTONICS
RESEARCH
Open Access

www.adpr-journal.com

Multipole Engineering of Attractive–Repulsive and Bending Optical Forces

Denis A. Kislov,* Egor A. Gurvitz, Vjaceslavs Bobrovs, Alexander A. Pavlov,
Dmitrii N. Redka, Manuel I. Marqués, Pavel Ginzburg, and Alexander S. Shalin

Focused laser beams allow controlling the mechanical motion of objects and can serve as a tool for assembling micro and nanostructures in space. While small particles mainly experience attractive gradient forces and repulsive radiation pressure, introducing additional flexibility suggests approaching new capabilities. Herein, optical forces acting on a high refractive index sphere in a focused Gaussian beam are analyzed and new regimes are revealed. Multipolar analysis allows separating an optical force into interception and recoil components, resulting in different mechanical actions. In particular, interplaying interception radial forces and multipolar resonances within a particle can lead to either trapping or antitrapping, depending on the system parameters. At the same time, the recoil force generates a significant azimuthal component along with an angular-dependent radial force. Those contributions enable enhancing either trapping or antitrapping and also introduce bending reactions. These effects are linked to the far-field multipole interference and, specifically, to asymmetric scattering patterns. The latter approach is extremely useful, as it allows assessing the nature of optomechanical motion by observing far-fields. Multipolar engineering of optical forces, being quite a general approach, is not necessarily linked to simple spherical shapes and paves a way to new possibilities in microfluidic applications, including sorting and microassembly.

1. Introduction

Optomechanical manipulation, demonstrated by Ashkin,[1] opened numerous venues in fundamental and applied science, e.g., in Refs. [2–4] Classical configurations of optical tweezers include a high numerical aperture objective, which focuses a laser beam into a small yet diffraction-limited spot. Typically, zero-order Gaussian beams are the preferable choice for achieving a stable trapping. In the case of subwavelength particles, the main contributing terms are the gradient force and radiation pressure—finding a balance between those two enables immobilizing an object. While this classical configuration has been widely explored and used nowadays, introducing new degrees of freedom in optomechanical manipulation is the subject of intensive research. Those investigations are partially inspired by new microfluidic applications, where fast sorting[5–7] and mixing[8] of colloidal substances are essential functions to have. Optomechanical tools are also frequently used in biological and biomedical investigations, where noninvasive in vivo manipulations are done with tissue-penetrating laser

Dr. D. A. Kislov, Dr. E. A. Gurvitz, Prof. A. S. Shalin
ITMO University
Kronverksky prospect 49, St. Petersburg 197101, Russia
E-mail: denis.a.kislov@gmail.com

Prof. V. Bobrovs, Dr. D. N. Redka, Prof. A. S. Shalin
Institute of Telecommunications
Riga Technical University
Azenes street 12, Riga 1048, Latvia

Dr. A. A. Pavlov, Prof. A. S. Shalin
Institute of Nanotechnology of Microelectronics
Russian Academy of Sciences
Moscow 119991, Russia

Dr. D. N. Redka
Saint Petersburg Electrotechnical University "LETI" (ETU)
5 Prof. Popova Street, 197376 St. Petersburg, Russia

Prof. M. I. Marqués
Departamento de Física de Materiales
IFIMAC and Instituto "Nicolás Cabrera"
Universidad Autónoma de Madrid
28049 Madrid, Spain

Prof. P. Ginzburg
School of Electrical Engineering
Tel Aviv University
Tel Aviv 69978, Israel

Prof. P. Ginzburg
Center for Photonics and 2D Materials
Moscow Institute of Physics and Technology
Dolgoprudny 141700, Russia

Prof. A. S. Shalin
Kotel'nikov Institute of Radio Engineering and Electronics
Russian Academy of Sciences (Ulyanovsk branch)
Goncharova Str.48, Ulyanovsk 432000, Russia

beams.[9–11] Furthermore, light-assisted targeted drug delivery (yet in vitro)[12,13] and biosensing[14] are areas where a flexible optomechanical manipulation can find use.

Enlarging a number of optomechanical degrees of freedom can be obtained with three fundamentally different approaches; at least the main reports in the field can be classified by the following logic. The first method is based on shaping a laser beam. One of the main experimental techniques here is to use holographic masks, either static[15,16] or reconfigurable[17,18] (spatial light modulators are typically used in the latter case). Holographic optical tweezers are used to trap multiple particles simultaneously.[19] Holographic masks are also used to generate non-Gaussian beams for optical trapping, e.g., Bessel beams[20,21] and beams with inherent orbital angular momentum.[22,23]

Another approach to flexible manipulation is to introduce auxiliary photonic structures, which assist configuring optical forces. Getting started with the goal of nanoscale localization of particles beyond the classical diffraction limit, the plasmonic tweezers concept[4,24] and related auxiliary tools were found to be an efficient approach for tailoring nanoscale mechanical motion with light.[25–28] For example, hyperbolic metamaterials and metasurfaces introduced a bunch of new effects, including tractor beams, antitrapping, and several others.[29–35] Other types of auxiliary optomechanical structures include metalenses,[36] laser-printed manipulators,[37] plasmonic Archimedes spiral lenses,[38] photonic hooks,[39,40] photonic nanojets[41–43] and many others.

The last method, to be mentioned in this context, is to shape a particle itself. In a vast majority of cases, optomechanical manipulation is conducted on spherical particles. Those are typically made of transparent low-index dielectric materials[44,45] or plasmonic metals.[46,47] In both cases, however, particles' polarizability is linked to its dipolar response and governs the interaction. Here, the balance between gradient forces and radiation pressure dictates the dynamics.[48] The latter can be quite complex due to nontrivial near fields, created by auxiliary structures.[49–51] However, high-index dielectric particles supporting a variety of Mie resonances[52,53] introduce new interaction channels beyond simple dipolar polarizability terms.[54,55] For example, coherent interaction between the electric and magnetic responses of silicon particles was shown to provide either pulling or pushing forces, depending on system parameters.[56] Sorting of silicon particles with laser beams was shown in the study by Shilkin et al.[57] Core–shell geometries allow designing multipole resonances within a structure.[58]

Careful tailoring of multipole interference can provide superior capabilities to control optical forces. Intuitively, a proper combination of multipoles can lead to quite arbitrary far-field scattering patterns. As a result, recoil forces can be flexibly engineered, though electromagnetic interactions in their complete form should be addressed—this is the goal of this article. The influence of conservative and nonconservative forces on particles' dynamics will be studied, and novel optomechanical effects delivered by different electric and magnetic multipoles will be introduced.

The article is organized as follows. After discussing the mathematical formulation of optical forces and linking them to multipolar expansion, conditions for trapping/antitrapping will be introduced. The detailed studies of force components will follow,

unraveling the emergence of new enhanced trapping, antitrapping, and bending phenomena.

2. Optical Forces in Multipolar Description

A typical setup under consideration is shown in **Figure 1**, showing an interaction of an optical beam with a particle. Typically, optical trapping is conducted with a focused Gaussian beam, which will be used here. The formalism, however, can be extended to an arbitrary waveform by applying a plane wave expansion (discussed below, e.g., in the study by Kashter et al.[59]). As plane wave scattering on a sphere has closed-form analytical solutions (Mie theory), optical force computation relying on the knowledge of self-consistent electromagnetic fields is also computationally efficient. Figure 1 shows the layout, which will be used for the subsequent investigations. A spherical particle is situated at the waist of a linearly polarized Gaussian beam. The forces will be analyzed at the focal plane, transverse to the propagation direction (Figure 1a). The emphasis will be done on far-field scattering diagram analysis (panel (b)), which will be responsible for controlling trapping/antitrapping conditions.

Time-averaged optical force ($\langle \mathbf{F} \rangle$) is calculated by integrating Maxwell's stress tensor ($\overset{\leftrightarrow}{\mathbf{T}}$) over a virtual surface (S) enclosing the particle.

$$\langle \mathbf{F} \rangle = \frac{1}{2} \text{Re} \oint_S \overset{\leftrightarrow}{\mathbf{T}} \cdot \mathbf{n} dS \tag{1}$$

where $\mathbf{n}$ is an outward normal to the enclosing surface. Hereinafter, we will use phasor notation, considering $e^{-i\omega t}$ as the time dependence. The medium enclosing the particle is assumed to be vacuum. In this case the stress tensor is given by

$$\overset{\leftrightarrow}{\mathbf{T}} = \varepsilon_0 \mathbf{E} \otimes \mathbf{E}^* + \mu_0 \mathbf{H} \otimes \mathbf{H}^* - \frac{1}{2}(\varepsilon_0 \mathbf{E} \cdot \mathbf{E}^* + \mu_0 \mathbf{H} \cdot \mathbf{H}^*)\overset{\leftrightarrow}{\mathbf{I}} \tag{2}$$

where $\mathbf{E} = \mathbf{E}_{inc} + \mathbf{E}_{sca}$ and $\mathbf{H} = \mathbf{H}_{inc} + \mathbf{H}_{sca}$ are total self-consistent electromagnetic fields, decomposed into the sum of incident and scattered contributions. As the shape and size of the enclosing surface does not affect the resulting force, as shown in Equation (1), a sphere with a radius ensuring far-field conditions on its boundary will be chosen. In this case, the total force can be decomposed into two contributions.

$$\langle {}^{\text{I}}\mathbf{F} \rangle = \lim_{r \to \infty} \oint_S \text{Re}\left[-\frac{1}{2}(\varepsilon_0 \mathbf{E}_{inc} \cdot \mathbf{E}_{sca}^* + \mu_0 \mathbf{H}_{inc} \cdot \mathbf{H}_{sca}^*)\mathbf{n}\right]dS$$

$$\langle {}^{\text{R}}\mathbf{F} \rangle = -\frac{1}{4}\lim_{r \to \infty} \oint_S \text{Re}[(\varepsilon_0 \mathbf{E}_{sca} \cdot \mathbf{E}_{sca}^* + \mu_0 \mathbf{H}_{sca} \cdot \mathbf{H}_{sca}^*) \cdot \mathbf{n}]dS$$

$$= -\frac{1}{2}\lim_{r \to \infty} \oint_S \text{Re}[(\varepsilon_0 \mathbf{E}_{sca} \cdot \mathbf{E}_{sca}^*) \cdot \mathbf{n}]dS \tag{3}$$

where $\langle {}^{\text{I}}\mathbf{F} \rangle$ (interception or extinction force) emerges from the interference between incident and scattered fields, whereas $\langle {}^{\text{R}}\mathbf{F} \rangle$ (recoil force) depends only on scattering. The latter is governed by multipolar interference, as shown in other studies.[60–63] The recoil force can be directly linked to the scattering diagram asymmetry.[64] Multipolar decomposition of the far-field is given by[65]
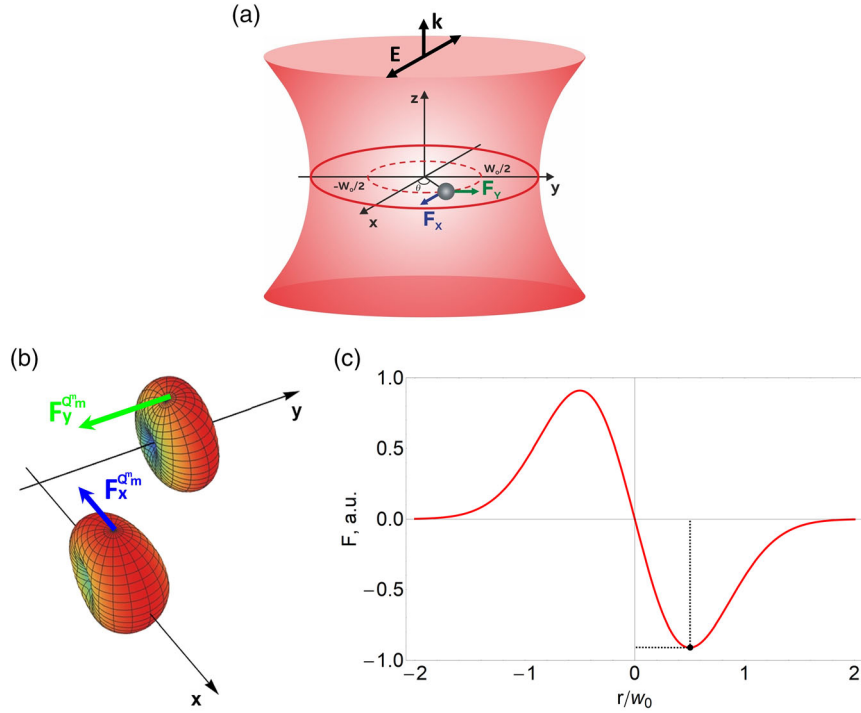
**ADVANCED
SCIENCE NEWS**
www.advancedsciencenews.com

**ADVANCED
PHOTONICS
RESEARCH**
www.adpr-journal.com

Figure 1. a) A particle in a Gaussian beam with w_0 beam waist + coordinate system. b) An example of scattered field formation by interfering magnetic dipole (m_y) and a magnetic quadrupole (Q^m_{xy}) for $\theta = 0$ and (Q^m_{yy}) for $\theta = \pi/2$. The asymmetry of the far-field scattering pattern leads to recoil forces shown by arrows. c) Transverse component of a gradient optical force, acting on a subwavelength dipolar particle. Black point indicates the position, where the subsequent calculations are carried out.

$$\begin{cases} \mathbf{E}_{sca}(\mathbf{r}) = \frac{k^2}{4\pi\varepsilon_0}\frac{e^{ikr_0}}{r_0}\left[\mathbf{n}\times(\mathbf{p}\times\mathbf{n}) + \frac{1}{c}(\mathbf{m}\times\mathbf{n}) + \frac{ik}{2}\mathbf{n}\times[\mathbf{n}\times(\mathbf{Q}^e\cdot\mathbf{n})] + \frac{ik}{2c}\mathbf{n}\times(\mathbf{Q}^m\cdot\mathbf{n})\right] \\ \mathbf{H}_{sca}(\mathbf{r}) = \frac{1}{\mu_0}\mathbf{B}_{sca}(\mathbf{r}) = \frac{1}{Z}\mathbf{n}\times\mathbf{E}_{sca}(\mathbf{r}) \end{cases} \quad (4)$$

where Z is the wave impedance and the expansion is made up of the quadrupole order. Multipolar moments (electric and magnetic dipoles, electric and magnetic quadrupoles, respectively) are given by

$$\mathbf{p} = \varepsilon_0\alpha_e\mathbf{E}_{inc}, \quad \mathbf{m} = \frac{\alpha_m}{\mu_0}\mathbf{B}_{inc}, \quad \mathbf{Q}^e = \varepsilon_0\alpha_{Q^e}\frac{\nabla\mathbf{E}_{inc} + \mathbf{E}_{inc}\nabla}{2},$$

$$\mathbf{Q}^m = \frac{\alpha_{Q^m}}{\mu_0}\frac{\nabla\mathbf{B}_{inc} + \mathbf{B}_{inc}\nabla}{2} \quad (5)$$

where the relation $(\nabla\mathbf{A} + \mathbf{A}\nabla)_{ij} = \partial_i A_j + \partial_j A_i$ is used. Polarizabilities are linked to Mie coefficients (a_1, a_2, b_1, and b_2[66]) as follows:

$$\alpha_e = i\frac{6\pi}{k^3}a_1, \quad \alpha_m = i\frac{6\pi}{k^3}b_1, \quad \alpha_{Q^e} = i\frac{40\pi}{k^5}a_2, \quad \alpha_{Q^m} = i\frac{40\pi}{k^5}b_2 \quad (6)$$

By substituting Equation (4) into (3), the following force decomposition is obtained:

$$\begin{cases} \langle F_i \rangle = \langle {}^I F_i \rangle + \langle {}^R F_i \rangle \\ \langle {}^I F_i \rangle = \frac{1}{2}\text{Re}\left[p_j\nabla_i E^*_{inc,j}\right] + \frac{1}{2}\text{Re}\left[m_j\nabla_i B^*_{inc,j}\right] + \frac{1}{4}\text{Re}\left[(Q^e)_{jk}\nabla_i\nabla_k E^*_{inc,j}\right] + \\ \quad + \frac{1}{4}\text{Re}\left[(Q^m)_{jk}\nabla_i\nabla_k B^*_{inc,j}\right] \\ \langle {}^R F_i \rangle = -\frac{k^4}{12\pi\varepsilon_0 c}\text{Re}\left[\varepsilon_{ijk}p_j m^*_k\right] - \frac{k^5}{40\pi\varepsilon_0}\text{Im}\left[(Q^e)_{ij}p^*_j\right] - \frac{k^5}{40\pi\varepsilon_0 c^2}\text{Im}\left[(Q^m)_{ij}m^*_j\right] - \\ \quad - \frac{k^6}{240\pi\varepsilon_0 c}\text{Re}\left[\varepsilon_{ijk}(Q^e)_{lj}(Q^m)^*_{lk}\right], \quad i,j,k \text{ can be } x, y, \text{ or } z \end{cases} \quad (7)$$

**ADVANCED
SCIENCE NEWS**

www.advancedsciencenews.com

**ADVANCED
PHOTONICS
RESEARCH**
Open Access

www.adpr-journal.com

This expression, as Equation (4), includes contributions up to quadrupole order, which is typically sufficient for describing interactions with submicrometer particles having refractive indices about 3−4. Equation (7) includes self-consistent electromagnetic fields and their spatial derivatives. It is worth noting that these expressions include cross-terms resulting from far-field interference of multipole contributions. Intuitively, their appearance can be understood by revising a simplified scenario. Consider optomechanical interactions with a Kerker particle, where constructive interference of electric and magnetic dipoles leads to the backscattering suppression. As a result of this rather dramatic scattering diagram reshaping (recall that a Gaussian beam can be decomposed into a sum of plane waves), new transverse forces, orthogonal to both gradient contribution and the radiation pressure, can emerge.[54]

To verify the contribution of different multipoles and justify the series truncation at the quadrupolar term in Equation (7), scattering efficiency of a silicon 140 nm-radius nanoparticle was calculated. From **Figure 2** we can see that, in this particular case, electric and magnetic octupoles (O^E and O^M) provide minor contribution to the interaction and they can be safely neglected. It is worth noting that in this investigation we use spherical multipoles as a basis. In this case, toroidal moments, which should be explicitly introduced in Cartesian expansion, are included by construction.

While the formalism of Equation (7) allows calculating optical forces, it can be further modified and brought to the form, where the link between scattering pattern asymmetry and recoil forces is evident. After some mathematical manipulations, the recoil force is given by

$$\langle {}^R\mathbf{F}\rangle = -\frac{1}{c}\oint_S \left(I_p + I_m + I_{Q^e} + I_{Q^m} + c\varepsilon_0 \mathrm{Re}\left[\mathbf{E}_{Q^e}\cdot\mathbf{E}_m^* + \mathbf{E}_{Q^m}\cdot\mathbf{E}_p^*\right]\right)\cdot\mathbf{n}\mathrm{d}S - $$
$$-\oint_S \left(\varepsilon_0\mathrm{Re}\left[\mathbf{E}_p\cdot\mathbf{E}_m^* + \mathbf{E}_{Q^e}\cdot\mathbf{E}_{Q^m}^* + \mathbf{E}_{Q^e}\cdot\mathbf{E}_p^* + \mathbf{E}_{Q^m}\cdot\mathbf{E}_m^*\right]\right)\cdot\mathbf{n}\mathrm{d}S \tag{8}$$

where far-field intensities I_p, I_m, I_{Q^e}, I_{Q^m} are obtained by substituting the electric field of the standalone multipole into the expression $I = \frac{c\varepsilon_0}{2}\mathbf{E}\cdot\mathbf{E}^*$ and all the subscripts correspond to the field scattered from the indicated multipole. Electric fields of multipoles can be either symmetric (do not change their sign when the vector $\mathbf{n}$ is replaced by $-\mathbf{n}$ in Equation (4) for $\mathbf{E}_p$, $\mathbf{E}_{Q^m}$) or antisymmetric (in the opposite case: $\mathbf{E}_m$, $\mathbf{E}_{Q^e}$). Consequently, multiplying the fields of different symmetry leads to an angular asymmetry in the cross-terms of Equation (8). Considering this behavior, and due to the fact that single multipoles have a symmetric intensity distribution, the first integral in Equation (8) vanishes, which leads to the simplified form of the recoil force.

$$\langle {}^R\mathbf{F}\rangle = -\oint_S \left(\varepsilon_0\mathrm{Re}\left[\mathbf{E}_p\cdot\mathbf{E}_m^* + \mathbf{E}_{Q^e}\cdot\mathbf{E}_{Q^m}^* + \mathbf{E}_{Q^e}\cdot\mathbf{E}_p^* + \mathbf{E}_{Q^m}\cdot\mathbf{E}_m^*\right]\right)\cdot\mathbf{n}\mathrm{d}S \tag{9}$$

Transverse components of the recoil optical force can be calculated by projecting vectorial force on the Cartesian coordinate system as follows:

$${}^R F_x^{pm} = -\frac{k^4}{12\pi\varepsilon_0 c}\mathrm{Re}\left[p_y m_z^* - p_z m_y^*\right]; \qquad {}^R F_y^{pm} = -\frac{k^4}{12\pi\varepsilon_0 c}\mathrm{Re}\left[p_z m_x^* - p_x m_z^*\right]$$

$${}^R F_x^{Q^e Q^m} = -\frac{k^6}{240\pi\varepsilon_0 c}\mathrm{Re}\left[\begin{array}{l}(Q^e)_{xy}(Q^m)_{xz}^* - (Q^e)_{xz}(Q^m)_{xy}^* + (Q^e)_{yy}(Q^m)_{yz}^* - (Q^e)_{yz}(Q^m)_{yy}^* + \\ +(Q^e)_{zy}(Q^m)_{zz}^* - (Q^e)_{zz}(Q^m)_{zy}^*\end{array}\right]$$

$${}^R F_y^{Q^e Q^m} = -\frac{k^6}{240\pi\varepsilon_0 c}\mathrm{Re}\left[\begin{array}{l}-(Q^e)_{xx}(Q^m)_{xz}^* + (Q^e)_{xz}(Q^m)_{xx}^* - (Q^e)_{yx}(Q^m)_{yz}^* + (Q^e)_{yz}(Q^m)_{yx}^* - \\ -(Q^e)_{zx}(Q^m)_{zz}^* + (Q^e)_{zz}(Q^m)_{zx}^*\end{array}\right]$$

$${}^R F_x^{Q^e p} = -\frac{k^5}{40\pi\varepsilon_0}\mathrm{Im}\left[(Q^e)_{xx}p_x^* + (Q^e)_{xy}p_y^* + (Q^e)_{xz}p_z^*\right]$$

$${}^R F_y^{Q^e p} = -\frac{k^5}{40\pi\varepsilon_0}\mathrm{Im}\left[(Q^e)_{yx}p_x^* + (Q^e)_{yy}p_y^* + (Q^e)_{yz}p_z^*\right]$$

$${}^R F_x^{Q^m m} = -\frac{k^5}{40\pi\varepsilon_0}\mathrm{Im}\left[(Q^m)_{xx}m_x^* + (Q^m)_{xy}m_y^* + (Q^m)_{xz}m_z^*\right]$$

$${}^R F_y^{Q^m m} = -\frac{k^5}{40\pi\varepsilon_0}\mathrm{Im}\left[(Q^m)_{yx}m_x^* + (Q^m)_{yy}m_y^* + (Q^m)_{yz}m_z^*\right]$$

$$(10)$$

Equation (10) provides explicit expressions underlining the link between the scattered pattern asymmetry and attraction/repulsion recoil forces.

The next step is to analyze the conditions, at which optical forces acting on a small particle are significantly different from the standard case, where only dipolar polarizability is taken into
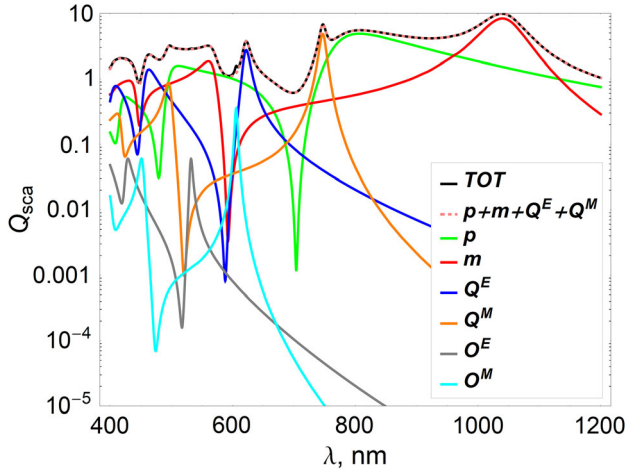
**ADVANCED
SCIENCE NEWS**

www.advancedsciencenews.com

**ADVANCED
PHOTONICS
RESEARCH**
Open Access

www.adpr-journal.com

Figure 2. Scattering efficiency of a silicon 140 nm-radius nanoparticle—total scattering efficiency and multipolar contributions (multipole abbreviations appear in the legend).

account. The typical trapping layout is shown in Figure 1. The following parameters are considered: the beam waist $w_0 = 5\,\mu m$ (loosely focused beam) and electrical field amplitude (at the beam's center) $E_0 = 10^6 [\text{V m}^{-1}]$. The beam is linearly polarized along x-axis and the Continuous Wave laser

wavelength is the subject to the forthcoming parametric study. Silicon nanoparticle is placed $r = w_0/2$ (black point in Figure 1a), whereas the azimuthal angle θ is a variable.

Angular spectral decomposition of a Gaussian beam is used to calculate the scattering pattern.[67] Fourier series for electric and magnetic fields is given as follows.

$$\mathbf{E}_{\text{inc}}(x, y, z) = \int\limits_{-\infty}^{+\infty} \int \hat{\mathbf{E}}(k_x, k_y; 0) e^{i(k_x x + k_y y + k_z z)} dk_x dk_y$$

$$\mathbf{H}_{\text{inc}}(x, y, z) = \int\limits_{-\infty}^{+\infty} \int \hat{\mathbf{H}}(k_x, k_y; 0) e^{i(k_x x + k_y y + k_z z)} dk_x dk_y \tag{11}$$

where $\hat{\mathbf{E}}(k_x, k_y; 0)$ and $\hat{\mathbf{H}}(k_x, k_y; 0)$ are the field amplitudes at the beam waist and k_i, $i = x, y, z$ are the wave vector components in the Cartesian coordinate system. For x-axis linearly polarized fundamental mode, the electric field $\mathbf{E}_{\text{inc}} = (E_x, 0, E_z)$ can be written in as

$$\hat{E}_x(k_x, k_y; 0) = E_0 \frac{w_0^2}{4\pi} e^{-(k_x^2 + k_y^2)\frac{w_0^2}{4}} \tag{12}$$

where the longitudinal z-component is insignificant (in more complex scenarios though it plays an important role[68]). Using Faraday's law, the magnetic field components are straightforwardly derived. Finally, the incident fields are given by

$$\mathbf{E}_{\text{inc}}(x, y, z) = \int\limits_{-\infty}^{+\infty} \int \hat{E}_x(k_x, k_y; 0) \frac{1}{k_z} [k_z \mathbf{n}_x - k_x \mathbf{n}_z] e^{i(k_x x + k_y y + k_z z)} dk_x dk_y$$

$$\mathbf{H}_{\text{inc}}(x, y, z) = Z^{-1} \int\limits_{-\infty}^{+\infty} \int \hat{E}_x(k_x, k_y; 0) \frac{1}{k k_z} [-k_x k_y \mathbf{n}_x + (k_x^2 + k_z^2)\mathbf{n}_y - k_y k_z \mathbf{n}_z] e^{i(k_x x + k_y y + k_z z)} dk_x dk_y \tag{13}$$

where $\mathbf{n}_i$, $i = x, y, z$ are unitary vectors.

3. Force Analysis

3.1. Antitrapping Conditions

Given the aforementioned plane wave decomposition of the beam, the Mie problem is solved and self-consistent electromagnetic fields are calculated. Then, those fields are introduced within Equation (7) and optical forces are calculated. **Figure 3** shows the results of the parametric study, where the transverse forces (F_x ($\theta; = 0$) and F_y ($\theta = \pi/2$)) are investigated as the function of the particle radius and the illumination wavelength. The colored areas on the map correspond to the antitrapping regime, whereas the grayscale parts show conditions where typical trapping takes place (recall the particle's position and coordinate system, defined in Figure 1). A 140 nm-radius silicon (material dispersion is from the study by Schinke et al.[69]) particle is used in the subsequent studies.

The examination of the results from Figure 3 shows the emergence of antitrapping regime, which is quite unusual to typical optical trapping scenarios, when low-contrast particles are in use. It is also worth noting that panels (a) and (b) are not entirely symmetric—this is the result of the well-defined polarization

of the incident beam, which affects the interference terms in Equation (10) quite differently. In other words, the asymmetry of F_x and F_y is a direct consequence of the recoil forces' radial component contribution. To prove this statement, we will consider the angular dependences of the interception and recoil forces for both, the radial and azimuthal components.

3.2. Antitrapping: Angular Dependence

As previously mentioned, linear polarization breaks the rotational symmetry of the problem and, hence, the optical force has an angular dependence. **Figure 4** shows this behavior, where we have made the transition between Cartesian and cylindrical coordinate systems. The surfaces have color gradients along θ and underline the non-uniform angular dependence. Overall, the optical force is not radial (typical conservative gradient force), which will lead to nontrivial particle's trajectories, as will be discussed later. This angular dependence of the radial force is especially pronounced for shorter wavelengths, where higher-order multipoles play a role (Figure 2).

The sign of the radial component of the force dictates whether the regime is trapping or antitrapping. As we will next show, the angular asymmetry of radial component, shown in Figure 4a, is a
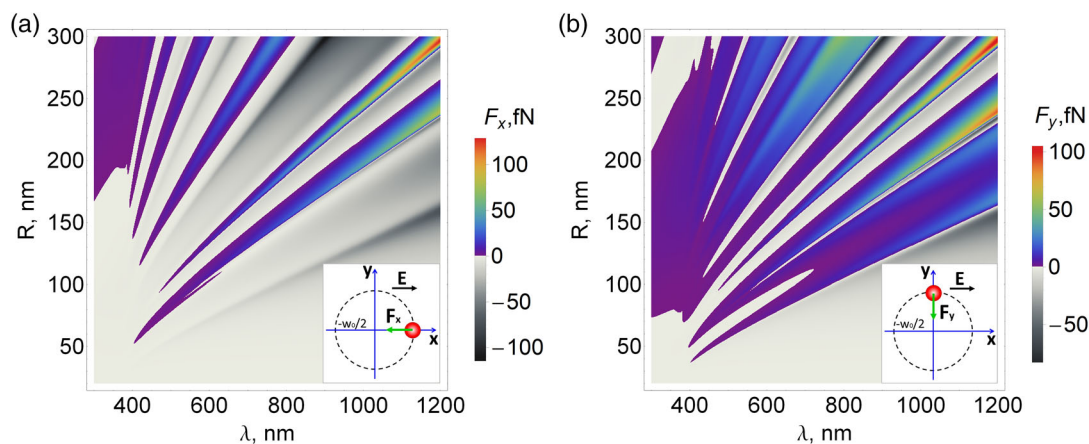
ADVANCED
SCIENCE NEWS

www.advancedsciencenews.com

ADVANCED
PHOTONICS
RESEARCH
Open Access

www.adpr-journal.com

Figure 3. Forces color maps, as a function of particle's radius and the illumination wavelength. a) F_x, $\theta = 0$ and b) F_y, $\theta = \pi/2$. Color regions correspond to the antitrapping regime. Grayscale areas correspond to conditions for an attraction force. The insets show the positions of the particle in the beam waist.
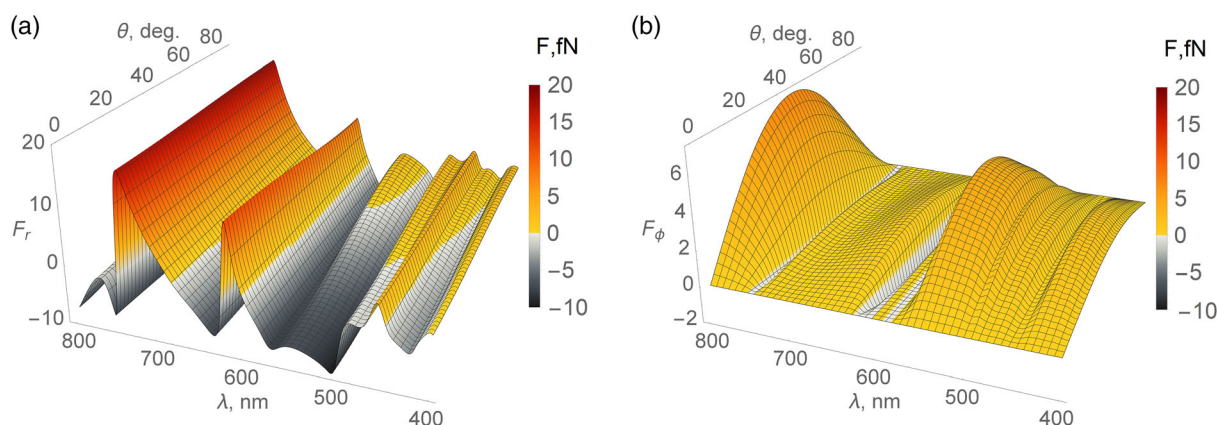

Figure 4. Force components' color surfaces. a) F_r and b) F_φ as a function of the illumination wavelength and angular position of the particle with respect to the beam polarization (Figure 1). For panel (a), color regions correspond to the antitrapping regime, whereas grayscale areas correspond to an attractive force. For panel (b), color regions correspond to the azimuthal component of the force that deflects the particle trajectory toward the y-axis and grayscale areas toward the x-axis (see Figure S1, Supporting Information).

direct consequence of the interplaying interception and recoil components. The azimuthal component, in contrast, has a symmetric angular distribution (relative to $\pi/4$ angle) and is responsible for the deviation of the particle's trajectory from radial motion. It drives the particle toward the x- or y-axis depending on wavelength (see Figure S2, Supporting Information).

Figure 5a shows the interception force in the focal plane, containing the beam waist. Interception forces are dominated by a gradient-derived radial component not depending on the angle.[70–72] Similar considerations were made by observing multipolar particle in a Bessel beam.[73] It is worth noting that the conservative nature of the interception force in the beam waist is determined exclusively by the structure of the electromagnetic field. A flat wave front in the waist plane causes the light pressure force acting on individual multipoles to be directed strictly along the beam propagation direction with no contribution to the transversal force. This effect does not depend qualitatively on the size and material of the particle, provided that the latter is spherical and isotropic.

Longitudinal forces can be compensated with several experimental techniques, including counter propagating beams and operation against the gravity. Other force components can be than disentangled from the longitudinal contribution and studied directly.

In optical tweezers, the intensity gradient value is negative at the point in space where the particle is localized in our study and, to obtain an antitrapping interception force in a dipole, a negative real part of the polarizability is needed. This is possible for plasmonic materials like silver but not for a low-contrast nanoparticle. However, it should be noted that, for the material considered in the present study, when more multipoles are excited, the sign of the interception force, determined by the sign of the corresponding standalone multipole polarizability (Equation (6)), may be negative, resulting in the existence of a repulsive force for nonmetallic materials (see details in Figure S3, Supporting Information).

The recoil force can also be divided into radial and azimuthal components.[62,63] Figure 5b shows that the angular dependence
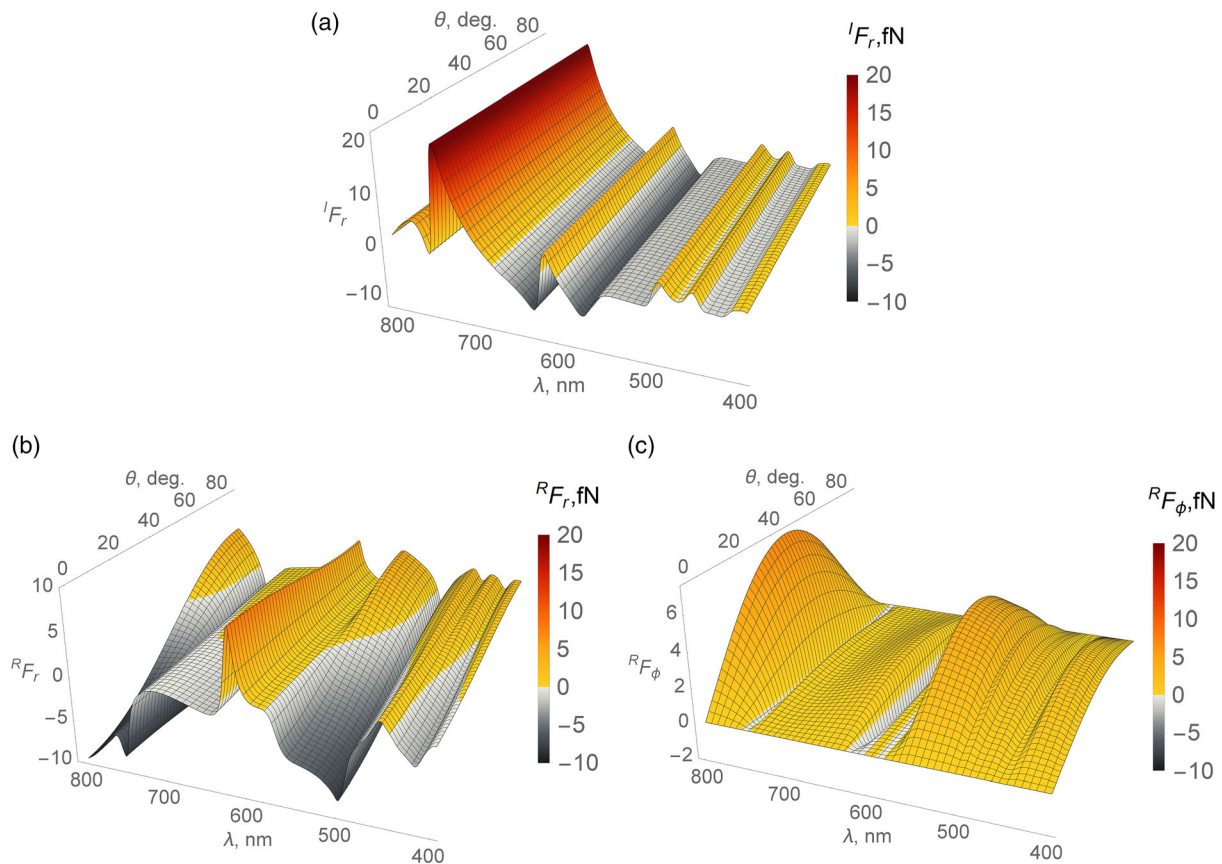
ADVANCED
SCIENCE NEWS

www.advancedsciencenews.com

ADVANCED
PHOTONICS
RESEARCH
Open Access

www.adpr-journal.com

Figure 5. Color surfaces of radial and azimuthal force components, as a function of the illumination wavelength and angular position of the particle. a) Interception force; b,c) recoil force. Color regions for (a) and (b) correspond to antitrapping regime and grayscale areas correspond to the conditions for an attractive force. For panel (c), color regions correspond to the azimuthal component of the recoil force that deflects the particle.

of the total radial force (Figure 4) is completely determined by the recoil force. The latter depends on the phase difference between pairs of interacting multipoles, as shown in Equation (9). Comparing Figures 4(b) and 5(c) we note that the recoil force is responsible for increasing the azimuthal component.

3.3. Multipole Analysis of Optical Forces

While the general behavior of interception and recoil forces was analyzed in the previous section, the contribution of multipoles will be analyzed next. **Figure 6**a,b shows the radial force spectra underlining the interception and recoil force term contributions. The areas of interest are those where the force is positive (antitrapping regime).

To get a closer inspection of the behavior shown in Figure 6, multipolar components will be investigated in detail. Several characteristic points have been selected (shown in Figure 6a,b) with vertical gray dashed lines). 1) Point "A" ($\lambda = 500$ nm), in the x-axis direction ($\theta = 0$) and y-axis direction ($\theta = \pi/2$), optical "trapping" is observed (the value of the net force is negative [see Figure 6a,b]), whereas the main contribution to the force is made by the recoil term (the value of the interception term can be neglected). 2) Point "B" ($\lambda = 555$ nm), optical "bending" is obtained. At $\theta = 0$, the trapping effect is observed, whereas at

$\theta = \pi/2$, the value of the net force changes sign to "plus" and the particle is pushed out of the beam. The sign of the net force in this case is determined by the recoil term (as the value of the interception term is always negative and does not depend on the angle θ). 3) Point "C" ($\lambda = 620$ nm), for any angle θ, the "antitrapping" effect is observed, whereas the contributions of the interception term and interference multipole terms to the value of the net force are comparable. 4) Point "D" ($\lambda = 700$ nm), there is also an angle-independent "anti-trapping" effect in this case defined by the conservative interception force component. The influence of the recoil term is insignificant.

Figure 6c,d shows the far-field patterns for conditions of points "A", "B", "C", and "D." Relationships between the angular asymmetry of the radiation patterns in the plane of the beam waist and the recoil force, arising from the interaction between the multipoles, can be seen. The asymmetry is the result of the fact that the integrand in Equation (9) can have both negative and positive values. The construction of an asymmetric radiation pattern of interacting multipoles is a good heuristic method for determining the direction of the recoil optical force vector, whereas Equation (9) is an alternative way to calculate its numerical value.

The nature of the optical forces described earlier is demonstrated on vector field maps, showing the spatial distribution
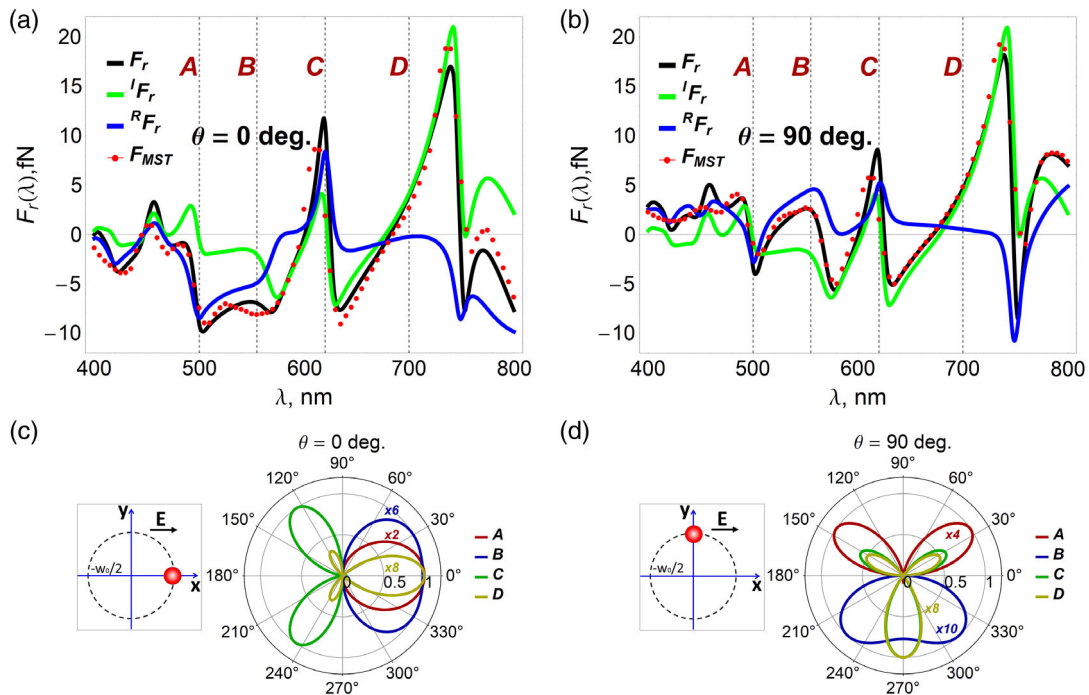
**ADVANCED
SCIENCE NEWS**

www.advancedsciencenews.com

**ADVANCED
PHOTONICS
RESEARCH**
Open Access

www.adpr-journal.com

Figure 6. Contribution of the radial interception (green) and recoil components (blue) to the total transversal force (black) acting on a silicon particle ($R = 140$ nm). a) $\theta = 0$ and b) $\theta = \pi/2$. The red dots show the net force obtained by integrating Maxwell's stress tensor (Equation (1)). Note how interception forces are angle independent and how both, negative and positive values, are possible. c,d) E-plane scattering patterns. The asymmetry is obtained by subtracting the intensity angular dependence in the x-axis negative direction from the intensity angular dependence in the x-axis positive direction (c) and y-axis (d). The scattering asymmetry determines the direction and magnitude of the recoil force. Particle's location and field polarization are indicated in the insets.
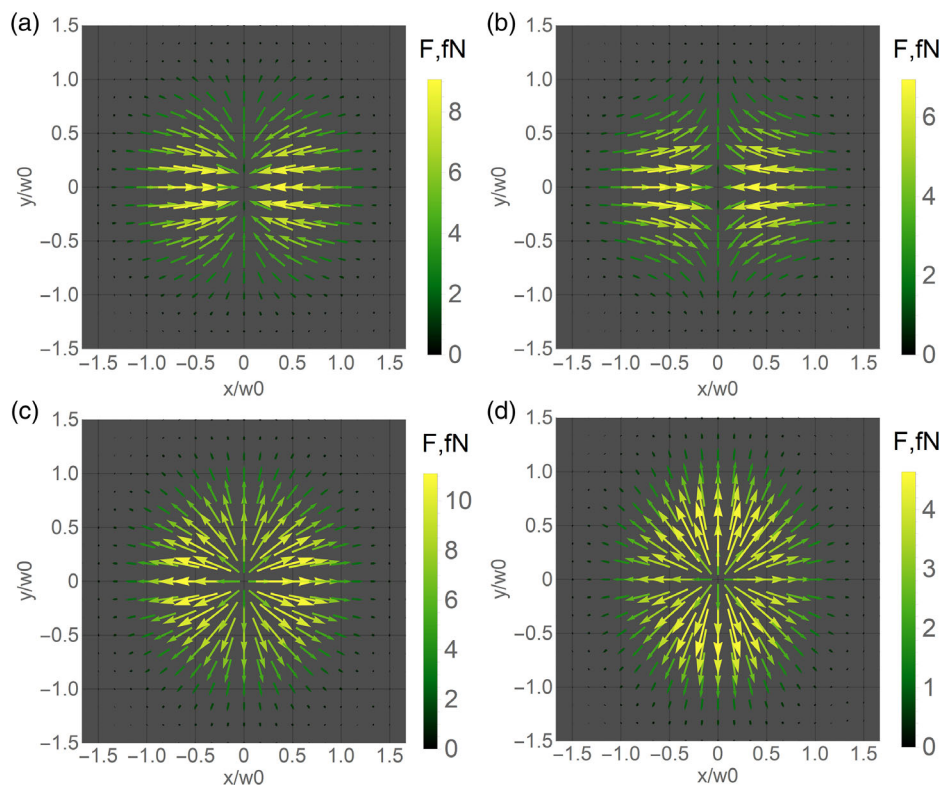

Figure 7. Spatial distribution of the net force in the xy plane for points "A," "B," "C," and "D."

of the net force F (**Figure 7**). For "C" and "D," the force is predominantly radial, whereas the forces calculated for points "A" and "B" include a significant azimuthal component (see angular distribution of azimuthal components of the net force in Figure S2a, Supporting Information). The radial component in these cases has a pronounced angular dependence and, for point B, the force changes sign, allowing for bending in the particle trajectory from a horizontal direction to a vertical route. The change in the sign of the total force is the result of the interaction between the interception and recoil terms (see Figure 5a,b) (see also vector maps of radial and azimuthal components of the net force in Figure S1 and S4, Supporting Information).

Next, we will investigate contributions of individual multipole components to the resulting optical force. **Figure 8** shows curves of different components from Equation (7). As can be seen from the comparison of Figure 8a,b, the antitrapping at point "D" is determined by the magnetic components of the optical force $^I F^m$ and $^I F^{Q^m}$.

Note that for the considered nanoparticle in the spectral window from 625 to 730 nm, the interception term also makes the main contribution to the net force. For example, at the wavelength of 630 nm, the trapping effect is observed, whereas the main contribution to this phenomenon is made by the electrical multipole terms of the optical forces $^I F^p$ and $^I F^{Q^e}$. Recall that in this case, when we consider the terms of the force corresponding to the interaction of individual multipoles with an external

electromagnetic field, its sign is determined by the phase of these multipole moments.

On the contrary, the trapping effect observed for point "A" is determined only by the interference terms $^R F^{Q^e p}$ and $^R F^{Q^m m}$ (see Figure 8c,d). As shown earlier, such a force can be associated with the asymmetry of the scattered radiation pattern.

Point "B" corresponds to an intermediate scenario where the contribution of both, interception and recoil terms, must be considered. However, as the magnitude and sign of the interception term do not depend on the angle θ, the change of the direction of the net force and the bending effect is determined by the dipole interference term $^R F^{pm}$. Point "C" also has contributions from interception and recoil terms, but, in this case, the dipole–quadrupole interference term $^R F^{Q^e p}$ is the one governing the force direction. It should be noted that this transverse antitrapping effect, obtained because of the two electric multipole interferences, is reported for the first time. In a Gaussian beam, the antitrapping effect was previously obtained only for interfering electric and magnetic dipoles.[54] Obtaining an antitrapping regime on the dipole–quadrupole interference of the same nature moments is inherent for high-index particles only.

We stress that the main difference between cases "C" and "B" is that, in the former case, as $^R F^{Q^e p}$ does not change its sign depending on the angle θ, the anti-trapping effect is always realized, whereas, in the last case, as the angular dependence of $^R F^{pm}$ is accompanied by a change of sign (Figure 8c,d), a bending
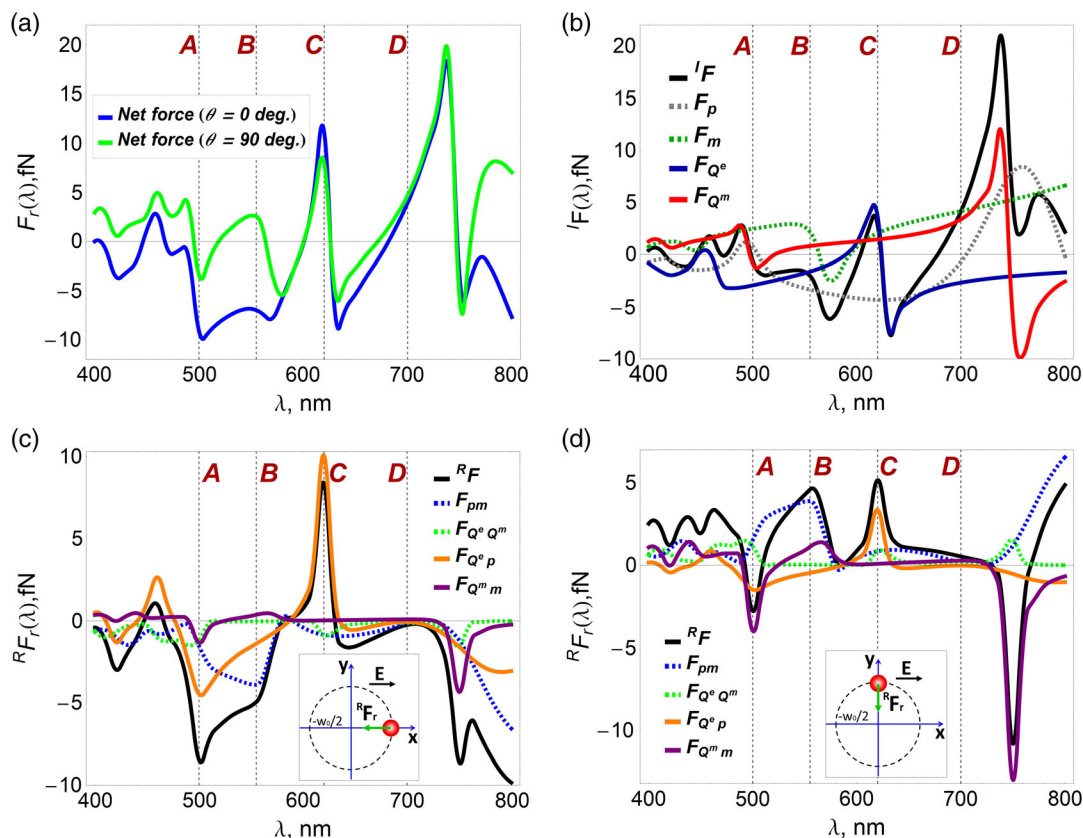

Figure 8. Radial component of the a) total force and multipole expansion of b) interception. c,d) Recoil optical force components, acting on a 140 nm silicon particle. Total force and multipolar contributions appear in legends: (c) F_r, $\theta = 0$ and d) F_r, $\theta = \pi/2$.

effect is induced with a trapping regime at $\theta = 0$ and antitrapping at $\theta = \pi/2$.

In addition, we should pay attention to the following. While the constructive interference between the terms in Equation (7) has quite a minor impact on the force behavior, the destructive one does take place and results in a complete nulling of the overall force. This occurs even though there is a moderately high gradient of the field intensity. The total optical force is equal to zero only for a set of wavelengths and at $\theta = 0$ and at $\theta = \pi/2$ (Figure 8a). There are also areas in which the net force approaches zero for any angle, although strictly not equal to zero. These are the regions with a wavelength of 600, 625, and 750 nm (see the spectral-angular dependences of the contours where net, interception, and recoil forces are zero in Figure S5, Supporting Information.).

4. Conclusion

The impact of higher-order multipoles on optomechanical interactions between focused laser beams and high-refractive-index particles has been investigated. It was shown that a proper balance between multipolar contributions allows controlling direction of optical forces, switching between trapping, antitrapping, and bending regimes almost on demand. In particular, it was shown that quadrupole moments are responsible for achieving antitrapping behavior. Furthermore, the interception force acting on a particle with a high refractive index can change sign depending on the incident light wavelength. For example, the transverse antitrapping regime governed by conservative interception forces (recoil forces in this case can be neglected) corresponds to the magnetic dipole and quadrupole moments of a particle. This effect is atypical for the classical optical tweezers, where the trapping regime is usually implemented. A transverse antitrapping regime can also emerge in the case of interplaying electrical modes only, where the recoil force dominates. Moreover, the very special regime of bending, particle's motion in a curved trajectory, could be also realized via different angle dependencies of the recoil and interception forces. All those regimes can be viewed in the light of far-field interference between higher-order multipoles, where asymmetry factor plays the key role.

Introduction of multipolar degrees of freedom into optomechanical interactions enlarges the capabilities of motion control at the nanoscale, opening a room of opportunities for new possible applications in optics, biology, medicine, and lab-on-a-chip platforms.

Supporting Information

Supporting Information is available from the Wiley Online Library or from the author.

Acknowledgements

Conflict of Interest

The authors declare no conflict of interest.

Data Availability Statement

Data sharing is not applicable to this article as no new data were created or analyzed in this study.

[1] A. Ashkin, J. M. Dziedzic, J. E. Bjorkholm, S. Chu, *Opt. Lett.* **1986**, *11*, 288.
[2] K. C. Neuman, S. M. Block, *Rev. Sci. Instrum.* **2004**, *75*, 2787.
[3] D. G. Grier, *Nature* **2003**, *424*, 810.
[4] M. L. Juan, M. Righini, R. Quidant, *Nat. Photonics* **2011**, *5*, 349.
[5] X. Qi, D. M. Carberry, C. Cai, S. Hu, Z. Yuan, H. Rubinsztein-Dunlop, J. Guo, *Biomed. Opt. Express* **2017**, *8*, 934.
[6] G. Tkachenko, E. Brasselet, *Nat. Commun.* **2014**, *5*, 1.
[7] X. Wang, S. Chen, M. Kong, Z. Wang, K. D. Costa, R. A. Li, D. Sun, *Lab Chip* **2011**, *11*, 3656.
[8] A. Canós Valero, D. Kislov, E. A. Gurvitz, H. K. Shamkhi, A. A. Pavlov, D. Redka, S. Yankin, P. Zemánek, A. S. Shalin, *Adv. Sci.* **2020**, *7*, 1903049.
[9] I. A. Favre-Bulle, A. B. Stilgoe, E. K. Scott, H. Rubinsztein-Dunlop, *Nanophotonics* **2019**, *8*, 1023.
[10] M. C. Zhong, X. Bin Wei, J. H. Zhou, Z. Q. Wang, Y. M. Li, *Nat. Commun.* **2013**, *4*, 1768.
[11] J. R. Staunton, B. Blehm, A. Devine, K. Tanner, *Opt. Express* **2017**, *25*, 1746.
[12] X. Liu, J. Yuan, D. Wu, X. Zou, Q. Zheng, W. Zhang, H. Lei, *Nanophotonics* **2020**, *9*, 611.
[13] S. T. Irawan D, *J. Biosens. Bioelectron.* **2014**, *05*, 1000159.
[14] P. Rodríguez-Sevilla, L. Labrador-Páez, D. Jaque, P. Haro-González, *J. Mater. Chem. B* **2017**, *5*, 9085.
[15] D. Barredo, V. Lienhard, P. Scholl, S. De Léséleuc, T. Boulier, A. Browaeys, T. Lahaye, *Phys. Rev. Lett.* **2020**, *124*, 023201.
[16] K. Kim, Y. Park, *Nat. Commun.* **2017**, *8*, 15340.
[17] X. Tang, X. Tang, F. Nan, Z. Yan, Z. Yan, *Nanoscale Adv.* **2020**, *2*, 2540.
[18] B. Cao, L. Kelbauskas, S. Chan, R. M. Shetty, D. Smith, D. R. Meldrum, *Opt. Lasers Eng.* **2017**, *92*, 70.
[19] D. G. Grier, Y. Roichman, *Appl Opt* **2006**, *45*, 880.
[20] H. Zhang, Y. Han, J. Wang, J. Guo, *J. Quant. Spectrosc. Radiat. Transf.* **2019**, *235*, 309.
[21] X. Li, J. Chen, Z. Lin, J. Ng, *Sci. Adv.* **2019**, *5*, eaau7814.
[22] X. Zou, Q. Zheng, D. Wu, H. Lei, *Adv. Funct. Mater.* **2020**, *30*, 2002081.
[23] A. D. Kiselev, D. O. Plutenko, *Phys. Rev. A* **2016**, *94*, 013804.
[24] D. G. Kotsifaki, S. N. Chormaic, *Nanophotonics* **2019**, *8*, 1227.

[25] A. S. Shalin, P. Ginzburg, P. A. Belov, Y. S. Kivshar, A. V. Zayats, *Laser Photonics Rev.* **2014**, *8*, 131.

[26] A. N. Koya, J. Cunha, T. L. Guo, A. Toma, D. Garoli, T. Wang, S. Juodkazis, D. Cojoc, R. Proietti Zaccaria, *Adv. Opt. Mater.* **2020**, *8*, 1901481.

[27] J. Berthelot, S. S. Aćimović, M. L. Juan, M. P. Kreuzer, J. Renger, R. Quidant, *Nat. Nanotechnol.* **2014**, *9*, 295.

[28] A. S. Shalin, S. V. Sukhov, *Plasmonics* **2013**, *8*, 625.

[29] D. A. Shilkin, E. V. Lyubin, I. V. Soboleva, A. A. Fedyanin, *JETP Lett.* **2014**, *98*, 644.

[30] A. Ivinskaya, N. Kostina, A. Proskurin, M. I. Petrov, A. A. Bogdanov, S. Sukhov, A. V. Krasavin, A. Karabchevsky, A. S. Shalin, P. Ginzburg, *ACS Photonics* **2018**, *5*, 4371.

[31] A. S. Shalin, S. V. Sukhov, A. A. Bogdanov, P. A. Belov, P. Ginzburg, *Phys. Rev. A – At. Mol. Opt. Phys.* **2015**, *91*, 063830.

[32] N. Kostina, M. Petrov, A. Ivinskaya, S. Sukhov, A. Bogdanov, I. Toftul, M. Nieto-Vesperinas, P. Ginzburg, A. Shalin, *Phys. Rev. B* **2019**, *99*, 125416.

[33] A. A. Bogdanov, A. S. Shalin, P. Ginzburg, *Sci. Rep.* **2015**, *5*, 15846.

[34] A. Ivinskaya, M. I. Petrov, A. A. Bogdanov, I. Shishkin, P. Ginzburg, A. S. Shalin, *Light Sci. Appl.* **2017**, *6*, e16258.

[35] N. A. Kostina, D. A. Kislov, A. N. Ivinskaya, A. Proskurin, D. N. Redka, A. Novitsky, P. Ginzburg, A. S. Shalin, *ACS Photonics* **2020**, *7*, 425.

[36] H. Markovich, I. I. Shishkin, N. Hendler, P. Ginzburg, *Nano Lett.* **2018**, *18*, 5024.

[37] I. Shishkin, H. Markovich, Y. Roichman, P. Ginzburg, *Micromachines* **2020**, *11*, 90.

[38] L. Cheng, X. Li, Z. Wang, P. Cao, X. He, T. Niu, *Appl. Sci.* **2019**, *9*, 674.

[39] A. S. Ang, A. Karabchevsky, I. V. Minin, O. V. Minin, S. V. Sukhov, A. S. Shalin, *Sci. Rep.* **2018**, *8*, 2029.

[40] M. Spector, A. S. Ang, O. V. Minin, O. V. Minin, I. V. Minin, I. V. Minin, A. Karabchevsky, *Nanoscale Adv.* **2020**, *2*, 2595.

[41] Y. Li, H. Xin, X. Liu, Y. Zhang, H. Lei, B. Li, *ACS Nano* **2016**, *10*, 5800.

[42] A. Kovrov, A. Novitsky, A. Karabchevsky, A. S. Shalin, *Ann. Phys.* **2018**, *530*, 1800129.

[43] D. Lu, M. Pedroni, L. Labrador-Páez, M. I. Marqués, D. Jaque, P. Haro-González, *Small* **2021**, *17*, 2006764.

[44] S. E. S. Spesyvtseva, K. Dholakia, *ACS Photonics* **2016**, *3*, 719.

[45] Z. Gong, Y. Le Pan, G. Videen, C. Wang, *J. Quant. Spectrosc. Radiat. Transf.* **2018**, *214*, 94.

[46] F. Han, T. Armstrong, A. Andres-Arroyo, D. Bennett, A. Soeriyadi, A. Alinezhad Chamazketi, P. Bakthavathsalam, R. D. Tilley, J. J. Gooding, P. J. Reece, *Nanoscale* **2020**, *12*, 1680.

[47] A. S. Urban, S. Carretero-Palacios, A. A. Lutich, T. Lohmüller, J. Feldmann, F. Jäckel, *Nanoscale* **2014**, *6*, 4458.

[48] S. Albaladejo, M. I. Marqués, M. Laroche, J. J. Sáenz, *Phys. Rev. Lett.* **2009**, *102*, 113602.

[49] A. S. Shalin, *JETP Lett.* **2010**, *91*, 636.

[50] S. V. Izmodenova, D. A. Kislov, M. G. Kucherenko, *Colloid J.* **2014**, *76*, 683.

[51] M. G. Kucherenko, D. A. Kislov, *J. Photochem. Photobiol. A Chem.* **2018**, *354*, 25.

[52] K. Baryshnikova, D. Filonov, C. Simovski, A. Evlyukhin, A. Kadochkin, E. Nenasheva, P. Ginzburg, A. S. Shalin, *Phys. Rev. B* **2018**, *98*, 165419.

[53] P. D. Terekhov, H. K. Shamkhi, E. A. Gurvitz, K. V. Baryshnikova, A. B. Evlyukhin, A. S. Shalin, A. Karabchevsky, *Opt. Express* **2019**, *27*, 10924.

[54] X. Xu, M. Nieto-Vesperinas, C. W. Qiu, X. Liu, D. Gao, Y. Zhang, B. Li, *Laser Photonics Rev.* **2020**, *14*, 1900265.

[55] N. O. Länk, P. Johansson, M. Käll, *Opt. Express* **2018**, *26*, 29074.

[56] H. Liu, M. Panmai, Y. Peng, S. Lan, *Opt. Express* **2017**, *25*, 12357.

[57] D. A. Shilkin, E. V. Lyubin, M. R. Shcherbakov, M. Lapine, A. A. Fedyanin, *ACS Photonics* **2017**, *4*, 2312.

[58] Z.-X. Xiang, X.-S. Kong, X.-B. Hu, H.-T. Xu, Y.-B. Long, H.-D. Deng, *Opt. Mater. Express* **2019**, *9*, 1105.

[59] Y. Kashter, E. Falek, P. Ginzburg, *J. Quant. Spectrosc. Radiat. Transf.* **2020**, *253*, 106887.

[60] A. Salandrino, S. Fardad, D. N. Christodoulides, *J. Opt. Soc. Am. B* **2012**, *29*, 855.

[61] X. Y. Duan, Z. G. Wang, *Phys. Rev. A* **2017**, *96*, 053811.

[62] J. Chen, J. Ng, Z. Lin, C. T. Chan, *Nat. Photonics* **2011**, *5*, 531.

[63] M. Nieto-Vesperinas, J. J. Sáenz, R. Gómez-Medina, L. Chantada, *Opt. Express* **2010**, *18*, 11428.

[64] A. Kiselev, K. Achouri, O. J. F. Martin, *Opt. Express* **2020**, *28*, 27547.

[65] R. E. Raab, *Multipole Theory in Electromagnetism*, Clarendonpress, Oxford, **2005**, 248.

[66] C. F. Bohren, D. R. Huffman, *Absorption and Scattering of Light by Small Particles*, Wiley-VCH, Hoboken NJ **1998**, 544.

[67] L. Novotny, B. Hecht, *Principles of Nano-Optics*, 2nd ed, Cambridge University Press, Cambridge, UK **2012**.

[68] A. V. Krasavin, P. Segovia, R. Dubrovka, N. Olivier, G. A. Wurtz, P. Ginzburg, A. V. Zayats, *Light Sci. Appl.* **2018**, *7*, 36.

[69] C. Schinke, P. C. Peest, J. Schmidt, R. Brendel, K. Bothe, M. R. Vogt, I. Kröger, S. Winter, A. Schirmacher, S. Lim, H. T. Nguyen, D. Macdonald, *AIP Adv.* **2015**, *5*, 067168.

[70] J. Du, C. H. Yuen, X. Li, K. Ding, G. Du, Z. Lin, C. T. Chan, J. Ng, *Sci. Rep.* **2017**, *7*, 18042.

[71] Y. Jiang, H. Lin, X. Li, J. Chen, J. Du, J. Ng, *ACS Photonics* **2019**, *6*, 2749.

[72] X. Yu, Y. Jiang, H. Chen, S. Liu, Z. Lin, *Phys. Rev. A* **2019**, *100*, 33821.

[73] G. Ha, H. Zheng, X. Yu, Z. Lin, *J. Opt. Soc. Am. B* **2020**, *37*, 67.